

# Imaging and Radiomics Study of Microvascular Infiltration of Primary Liver Cancer Using a Seven-point Pathological Sampling Method

**Xialing Huang**

The First Affiliated Hospital of Guangxi Medical University

**Jieqin Wei**

Guangxi Medical University

**Xinping Ye**

The First Affiliated Hospital of Guangxi Medical University

**Zili Lv**

The First Affiliated Hospital of Guangxi Medical University

**Ling Zhang**

The First Affiliated Hospital of Guangxi Medical University

**Muliang Jiang**

The First Affiliated Hospital of Guangxi Medical University

**Yidi Chen**

Guangxi Medical University

**Fang Wang**

Huiying Medical Technology (Beijing)

**Yuwei Xia**

Huiying Medical Technology (Beijing)

**Liling Long** (✉ [cjr.longliling@vip.163.com](mailto:cjr.longliling@vip.163.com))

The First Affiliated Hospital of Guangxi Medical University

---

## Research Article

**Keywords:** primary liver cancer, pathology, seven-point sampling, microvascular infiltration, radiomics

**Posted Date:** December 10th, 2020

**DOI:** <https://doi.org/10.21203/rs.3.rs-110032/v1>

**License:** © ⓘ This work is licensed under a Creative Commons Attribution 4.0 International License.

[Read Full License](#)

# Abstract

**Purpose** In this study, the aim was to assess the imaging features and radiomics of microvascular infiltration (MVI) of primary liver cancer (PLC) under the control of a seven-point pathological sampling method.

**Methods** The data of 37 patients with PLC who underwent surgical resection in our hospital from October 2018 to September 2019 were retrospectively collected. Postoperative pathological specimens were collected using a seven-point sampling method to determine the presence of MVI. Preoperative CT and MRI scans were performed to characterize the tumors. Findings from the imaging studies were imported into the radiomics platform, and 70% and 30% of the data were randomly assigned to the training and validation sets, respectively. Lastly, support vector machine (SVM) classifiers were used to classify liver lesions into their respective pathological types.

**Results** Differences in tumor morphology and satellite lesions were statistically significant between the MVI positive and MVI negative groups on CT images. On MRI, there were statistically significant differences between the MVI positive and MVI negative groups in peripheral enhancement of the arterial phase (AP) and peripheral low signal in the hepatobiliary phase (HBP). In the radiomics analysis, the imaging features extracted from the AP had strong predictive power in both groups (CT and MRI). For the phase images, 15 and 12 valuable features from CT and MRI were selected to develop the radiomics signature, respectively. The AUCs of the training set were 0.965 (sensitivity: 0.979; specificity: 0.931; precision: 0.939) and 0.962 (sensitivity: 0.963; specificity: 0.897; precision: 0.923), the validation set were 0.842 (sensitivity: 0.967; specificity: 0.733; precision: 0.714) and 0.769 (sensitivity: 0.846; specificity: 0.727; precision: 0.727). The PVP also performed well on CT (AUC: 0.851/0.891) and MRI (AUC: 0.886/0.846). The predictive power was not enhanced by combining the features of multi-phase images.

**Conclusions** This was a controlled study on preoperative CT and MRI imaging and radiomics based on a seven-point pathological sampling method can avoid false-negative results caused by traditional pathological sampling. The imaging analysis results obtained and the radiomics prediction model established in this study may be more accurate than conventional models.

## Introduction

PLC is one of the most common malignant tumors in the world. Due to substantial advances in diagnostic imaging in recent years, the early detection rates of PLC has increased globally, leading to improved survival rates. Currently, resection of the primary tumor and liver transplantation are the two primary surgical strategies used for PLC, yet the 5-year recurrence rate after surgery is high at 35–70% [1]. MVI is an essential factor that affects the postoperative recurrence and prognosis of cancer patients [2], including those with PLC [3, 4]. Microvascular infiltration refers to the presence of tumor cells in the vascular space lined by endothelial cells, which primarily consists of portal vein branches (including intracapsular vessels) [5].

At present, the gold standard for diagnosing PLC MVI is observation via postoperative pathological microscopy [6]. The periphery of PLC tumors is the representative region of biological tumor behavior [7]. According to the 2017 edition of the guidelines for the diagnosis and treatment of PLC, for a single tumor with a maximum diameter of > 3 cm, the seven-point baseline sampling method should be used for the pathological assessment of gross specimens [8]. In a previous retrospective analysis on preoperative imaging of MVI, the seven-point sampling method and image location were not compared when using the pathological gold standard [9, 10]. However, some patients who actually have MVI may have false-negative results due to the lack of pathologically-determined MVI, leading to inaccurate findings.

In this study, image control was performed on postoperative pathology using a seven-points sampling method to accurately analyze the preoperative imaging manifestations of PLC MVI and to conduct radiomics modeling.

## Materials And Methods

### Clinical data

The data from 37 patients diagnosed with PLC who underwent surgical resection in our hospital from October 2018 to September 2019 were collected. The inclusion criteria included the following: a single primary lesion in the liver with a diameter of > 3 cm, as examined by CT and MRI within one month before surgery, along with PLC determined by postoperative pathology. The exclusion condition was a single primary lesion diameter of  $\leq 3$  cm. Preoperative interventional examinations were performed, and the lesions were multiple intrahepatic diffuse PLC. In this experiment, hepatobiliary surgeons performed intraoperative ligation and localization of lesion specimens. In Fig. 1a, one suture line represented the front of the human body, and two sutures represented the right side of the human body. The largest section of the lesion was incised along the transverse plane of the body (Fig. 1a).

### Pathological materials

Postoperative gross specimens of all enrolled patients were collected using the seven-point baseline sampling method at which 12, 3, 6, and 9 o'clock positions of the maximum section of the tumor were sampled. The samples were collected at the junction of the carcinoma and para-carcinoma liver tissue at 1:1 (A, B, C, and D); at least one piece was taken from inside the tumor (E); and one piece of liver tissue was collected from the tumor margins  $\leq 1$  cm (near the tumor) and > 1 cm (far near the tumor) (F,G), as shown in Fig. 1b. The pathological diagnosis was reported according to the seven points of sampling, which were jointly completed by two pathologists with more than 12 years of combined work experience. According to the postoperative pathological findings, 37 patients were divided into the MVI positive group and MVI negative group. The patients with MVI at one or more of the sampling points were defined as the MVI positive group, while those without MVI were defined as the MVI negative group. Since MVI tends to occur at the junction between the tumor and healthy liver tissues, this study only conducted statistical analyses on the results of A, B, C, and D.

### Imaging data

*CT:* Thirty-three patients underwent enhanced upper abdominal CT. Twenty cases were scanned using the Siemens dual-source spiral CT (SOMATOM Definition Flash, Germany), and the scanning parameters were: thickness of 1.5 mm, pitch of 0.8, tube voltage of 120 kV, and tube current of 210 mAs. The GE 64-slice spiral CT scanner (Light Speed VCT, Germany) was used in 13 cases. The scanning parameters were as follows: thickness of 1.25 mm, pitch of 0.984, tube voltage of 100 kV, tube current of 400 mAs. First, the patients underwent a scan of the whole liver, followed by enhanced scanning. A contrast agent was used in the imaging sessions (Iopromide, 300 mgI/mL, Germany Bayer Healthcare Co.), with a dosage of 1.5 mL/kg and blood flow rate of 3 mL/s through the superficial vein on the elbow with a double-barrel high-pressure syringe. At 30 s, 60 s, and 120 s post-injection, the arterial phase, portal vein phase, and delayed phase were scanned, respectively. According to the pathological results, 33 patients were divided into the MVI positive group and MVI negative group. The size, shape (round/irregular), and presence of satellite lesions of the tumor were analyzed by comparing the pathological specimens of the patients with the CT images.

*MRI:* Twenty-three patients underwent enhanced MR imaging with 10 mL Gd-EOB-DTPA at 0.25 mmol/mL (Germany Bayer Healthcare Co.) using the Siemens Verio 3.0 T MRI scanner (Germany), with a 12-channel body phased-array coil. Gd-EOB-DTPA was administered as a bolus injected at a rate of 1 mL/s through the cubital vein followed by a 20 mL saline chaser administered at the same rate. The scanning parameters of T1WI volume interpolated body examinations (VIBE) included the following: repetition time (TR) of 3.9 ms, echo time (TE) of 1.4 ms, flip angle of 9° (30° in hepatobiliary phase), field of view (FOV) of 350 mm, matrix of 168 × 320, voxel size of 1.6 × 1.1 × 4.5 mm, signal to noise ratio (SNR) of 1.00, and section thickness of 4.5 mm. The scanning parameters of T2WI using the BLADE technique were TR 2930 ms, TE 189 ms, FOV 400 mm, voxel size 1.3 × 1.3 × 6.0 mm, SNR 1.00, and 6 mm section thickness. The scanning parameters of diffusion-weighted imaging (DWI) were as follows: TR of 9000 ms, TE of 66 ms, FOV of 420 mm, matrix of 80 × 148, voxel size of 3.5 × 2.8 × 6.0 mm, SNR of 1.00, and section thickness of 6 mm. Delay phase scanning was performed at 5, 10, and 20 min after the administration of Gd-EOB-DTPA.

The points (A, B, C, and D) of 23 patients were divided into the MVI positive group and MVI negative group, based on the pathological findings. Next, the corresponding points on the MRI images were compared, and the tumor boundaries (clear/fuzzy), peripheral enhancement in AP, and peripheral low signal in HBP were analyzed.

## **Radiomics methods**

### **Image segmentation**

A total of 13 patients who were examined by CT before the operation and confirmed by pathology after the operation to have MVI were selected for the radiomics analysis, along with five patients who were examined by the same imaging tool before surgery and confirmed by pathology to have no MVI were randomly selected. The points (A, B, C, and D) of 18 patients (72 points in total) were selected for image segmentation under pathological control.

Eleven patients, who had undergone MRI examinations before surgery and were confirmed to have MVI by post-surgery pathology, were selected. Four patients who had been examined by the same imaging tool before surgery and were confirmed to have no MVI were randomly selected. The points (A, B, C, and D) of 15 patients (60 points in total) were selected for image segmentation under pathological control.

The regions of interest (ROI) were drawn in the cross-section of the corresponding images of the pathological specimens, using a rectangle similar to the shape of the pathological specimen. The ROI was selected from the AP, portal venous phase (PVP), and delayed phase (DP) of CT images (MRI added the HBP), and was delineated by a junior radiologist who had two years of work experience. Each segmentation was re-examined by a senior radiologist with more than 11 years of work experience (Figs. 2 and 3).

### **Radiomic feature extraction and machine learning**

This study included 18 CT cases and 15 MRI cases. The former included arterial, venous, and delayed phase images, while the latter included more hepatobiliary phase images. All images were transferred into the radiomics platform of Huiying Medical Technology (Beijing, China). Radiomic features were subdivided into first-order, shape, texture, and filter-based features, accounting for 1,395 in total. The features were extracted from liver lesions outlined in all sections of each phase image. Only a small number of patients included in this study developed tumor invasion. Therefore, before dimensionality reduction of the data was performed, the sample equilibrium was carried out using the SMOTE (Synthetic Minority Oversampling Technique) algorithm. The Variance Threshold, Select K Best, and Lasso methods were used to reduce the dimensionality of features and filter out the imaging features with high diagnostic efficiency in each phase. In total, 70% of the data were randomly assigned to the training set, while the other 30% to the validation set. In addition, support vector machine (SVM) classifiers were used to classify liver lesions into the respective pathological types.

### **Statistical analysis**

The prediction performance of the SVM in each phase image was evaluated by receiver operating characteristic (ROC) curves of the training set, as well as the validation set. Sensitivity, specificity, precision, and 95% CI were calculated to diagnose the SVM model. SPSS version 22.0 software (IBM, Chicago, IL, USA) was used for statistical analysis. Between-group comparisons were conducted with the chi-squared test for categorical variables and the independent sample *t*-test for continuous variables. Multivariate analysis was performed using logistic regression. Significance was set at  $p < 0.05$ .

## **Results**

### **Clinical features**

In total, 37 patients (30 males and seven females) aged from 33 to 74 years old were enrolled in this study, including 35 patients with hepatocellular carcinoma (HCC) and two patients with combined hepatocellular carcinoma and cholangiocarcinoma (cHCC-CC). Postoperative pathology was used to

confirm 16 cases (24 points in total) in the MVI positive group and 21 cases in the MVI negative group. Gender, age, hepatitis b surface antigen (HBsAg), alpha-fetoprotein (AFP), des-γ-carboxy Prothrombin (DCP), and liver cirrhosis were compared among the two groups, and the differences were not statistically significant (Table 1).

Table 1  
Comparison of clinical characteristics between the MVI positive and MVI negative groups.

Group	Gender (M/F)	Age (Years)	HBsAg <sup>+</sup> (Cases)	AFP <sup>+</sup> (Cases)	DCP <sup>+</sup> (Cases)	Liver cirrhosis (Cases)
MVI <sup>+</sup>	14/2	46.7 ± 8.1	15/16	14/16	14/16	7/16
MVI <sup>-</sup>	16/5	51.8 ± 12.1	19/21	14/21	18/21	11/21
t/χ <sup>2</sup>	0.757	-1.456	0.131	2.141	0.025	0.271
P	0.674	0.071	1.000	0.248	1.000	0.743

AFP, alpha-fetoprotein; DCP, des-γ-carboxy Prothrombin; HBsAg, Hepatitis B surface antigen; MVI, microvascular infiltration.

### Imaging analysis

In this study, 33 patients underwent preoperative CT examinations. There were 15 cases in the MVI positive group, and 14 cases with the maximum tumor diameter of ≥ 5 cm. The tumors were irregularly shaped in 10 cases. Satellite lesions were observed around the tumor in eight of the cases. There were 18 cases in the MVI negative group, and 12 cases with the maximum tumor diameter ≥ 5 cm. The tumors were irregularly shaped in four of the cases. Satellite lesions were observed around the tumor in one case (Table 2). Univariate analysis revealed that the difference between the two groups was statistically significant in the two factors of irregular tumor morphology and satellite lesions around the tumor. The multivariate logistic regression analysis showed that the model was statistically significant ( $P=0.010$ ).

Table 2  
Comparison of CT image features between MVI positive and MVI negative groups.

Group	Diameter $\geq$ 5 cm (Cases)	Irregular shape (Cases)	Satellite lesions (Cases)
MVI <sup>+</sup>	14/15	10/15	8/15
MVI <sup>-</sup>	12/18	4/18	1/18
Chi-square			
$\chi^2$	3.481	6.671	9.416
<i>P</i>	0.095	0.015*	0.004*
Logistic regression			
OR	0.333	0.750	0.083
<i>P</i>	0.376	0.749	0.076
95% CI	0.029-3.800	0.087–6.468	0.005–1.294
OR, odds ratio; 95% CI, 95% confidence interval; MVI, microvascular infiltration. * <i>P</i> < 0.05 was statistically significant.			

Next, 23 patients underwent preoperative MRI examinations. In the MVI positive group, there were 12 cases, with an MVI total of 24/48 points, including 20 points with a fuzzy boundary. There were 11 points of enhancement around the tumor in the AP and 16 points of low signal around the tumor in the HBP. In the MVI negative group, there were 11 cases with a total of 44 points, including six points with a fuzzy boundary. There were two points of enhancement around the tumor in the AP and four points of low signal around the tumor in the HBP (Table 3). Univariate analysis showed that the differences between the three factors, including fuzzy tumor boundary, peripheral enhancement in the AP, and peripheral low signal in the HBP, were statistically significant between the two groups. The multivariate logistic regression analysis showed that the model was statistically significant (*P* = 0.017).

Table 3  
Comparison of MRI image features between the MVI positive and MVI negative groups.

Group	Fuzzy boundary (points)	Peripheral enhancement in AP (points)	Low peripheral signal in HBP (points)
MVI <sup>+</sup>	20/48	11/48	16/48
MVI <sup>-</sup>	6/44	2/44	4/44
Chi-square			
$\chi^2$	8.897	6.385	7.930
<i>P</i>	0.005*	0.015*	0.006*
Logistic regression			
OR	0.368	0.455	0.800
<i>P</i>	0.268	0.488	0.853
95% CI	0.063–2.155	0.049–4.214	0.076–8.474
OR, odds ratio; 95% CI, 95% confidence interval; AP, arterial phase; HBP, arterial phase; MVI, microvascular infiltration. * <i>P</i> < 0.05 was statistically significant.			

## Machine learning

In total, 15, 11, and 15 kinds of effective features were extracted from the AP, PVP, and DP of the enhanced CT images, which were correlated with MVI. In addition, 12, 12, 13, and 9 kinds of effective features were extracted from the AP, PVP, DP, and HBP of MRI images, which were associated with MVI (Tables 4 and 5). The SVM classifier was used for machine learning, and the ROC curve of the model established in each phase, along with the multi-phase of CT and MRI, are shown in Fig. 4. The evaluation indexes of each phase model are shown in Table 6.

Table 4  
Coefficient values of the effective texture features in each phase of CT.

Image	Effective texture features	Coefficient values
AP	LongRunHighGrayLevelEmphasis_glrIm_original	0.395312482
		0.63
		0.712 ± 0.087
	SmallAreaLowGrayLevelEmphasis_glszm_logarithm	0.338164078
	LowGrayLevelZoneEmphasis_glszm_gradient	0.052444914
	Skewness_firstorder_wavelet-LHL	0.492845701
	Median_firstorder_wavelet-LHL	0.111711586
	Mean_firstorder_wavelet-LHL	0.158794207
	lmc1_glcm_wavelet-LHL	0.266508583
	SizeZoneNonUniformityNormalized_glszm_wavelet-LHL	0.294768575
	Mean_firstorder_wavelet-HHH	0.124303087
	ShortRunEmphasis_glrIm_wavelet-HHH	0.179997815
	SizeZoneNonUniformityNormalized_glszm_wavelet-HHH	0.156238439
	SmallAreaLowGrayLevelEmphasis_glszm_wavelet-HHH	0.398870007
PVP	DependenceEntropy_gldm_wavelet-HHL	0.243208987
	RunLengthNonUniformityNormalized_glrIm_wavelet-HHL	0.480960455
	SizeZoneNonUniformity_glszm_wavelet-HHL	0.045803467
	LongRunHighGrayLevelEmphasis_glrIm_original	0.081541618
	Kurtosis_firstorder_gradient	0.143384202
	Skewness_firstorder_wavelet-LHL	0.245395915
	SmallAreaLowGrayLevelEmphasis_glszm_wavelet-HLL	0.156655457
	Correlation_glcm_wavelet-LLH	0.335867542
	Kurtosis_firstorder_wavelet-HLH	0.203602351
	ClusterShade_glcm_wavelet-HLH	0.094397774
	MaximumProbability_glcm_wavelet-HLH	0.176011943
	GrayLevelVariance_glszm_wavelet-HHH	0.230122655
	SizeZoneNonUniformityNormalized_glszm_wavelet-HHH	0.353082167

<b>Image</b>	<b>Effective texture features</b>	<b>Coefficient values</b>
	Contrast_ngtdm_wavelet-LLL	0.401524614
DP	DependenceVariance_gldm_wavelet-LHL	0.203050077
	RunVariance_gIrlm_wavelet-LHL	0.172656629
	Mean_firstorder_wavelet-LHH	0.032214474
	SizeZoneNonUniformityNormalized_glszm_wavelet-HLL	0.008589922
	SizeZoneNonUniformity_glszm_wavelet-HLL	0.188668901
	Correlation_glcm_wavelet-LLH	0.19706693
	DependenceNonUniformityNormalized_gldm_wavelet-LLH	0.342762485
	Mean_firstorder_wavelet-HLH	0.08030132
	GrayLevelNonUniformityNormalized_glszm_wavelet-HLH	0.474383186
	Skewness_firstorder_wavelet-HHH	0.52948975
	GrayLevelNonUniformityNormalized_glszm_wavelet-HHH	0.082980349
	LowGrayLevelZoneEmphasis_glszm_wavelet-HHH	0.292402573
	SmallAreaLowGrayLevelEmphasis_glszm_wavelet-HHL	0.15582439
	ClusterProminence_glcm_wavelet-LLL	0.322785896
	SmallAreaLowGrayLevelEmphasis_glszm_wavelet-LLL	0.445709468
ALL	DependenceVariance_gldm_original	0.191867222
	LargeAreaHighGrayLevelEmphasis_glszm_original	0.340380979
	lmc1_glcm_logarithm	0.200347359
	DependenceNonUniformityNormalized_gldm_logarithm	0.332917108
	Kurtosis_firstorder_gradient	0.139728301
	SizeZoneNonUniformityNormalized_glszm_gradient	0.018888231
	LargeAreaLowGrayLevelEmphasis_glszm_gradient	0.253013627
	ShortRunLowGrayLevelEmphasis_gIrlm_square	0.164090018
	DependenceVariance_gldm_squareroot	0.035784746
	LowGrayLevelEmphasis_gldm_squareroot	0.057525549
	Skewness_firstorder_lbp-2D	0.187104783
	Kurtosis_firstorder_wavelet-LHL	0.055104213

<b>Image</b>	<b>Effective texture features</b>	<b>Coefficient values</b>
	ClusterShade_glcm_wavelet-LHL	0.276222851
	DependenceVariance_gldm_wavelet-LHL	0.136782551
	SizeZoneNonUniformityNormalized_glszm_wavelet-LHL	0.075269333
	10Percentile_firstorder_wavelet-LHH	1.03086679
	Complexity_ngtdm_wavelet-LHH	0.261112868
	90Percentile_firstorder_wavelet-HLL	0.600365129
	LargeDependenceHighGrayLevelEmphasis_gldm_wavelet-HLL	0.090418491
	SizeZoneNonUniformityNormalized_glszm_wavelet-HLL	0.100681752
	TotalEnergy_firstorder_wavelet-LLH	0.078160506
	Contrast_ngtdm_wavelet-LLH	0.1271655
	90Percentile_firstorder_wavelet-HLH	0.353559564
	ShortRunEmphasis_glrIm_wavelet-HLH	0.301562346
	Contrast_ngtdm_wavelet-HLH	0.392353718
	SizeZoneNonUniformityNormalized_glszm_wavelet-HHH	0.062625442
	GrayLevelNonUniformityNormalized_glszm_wavelet-HHL	0.039812992
	GrayLevelNonUniformityNormalized_glszm_wavelet-LLL	0.219331932
	Contrast_ngtdm_wavelet-LLL	0.202699468
AP, arterial phase; PVP, portal venous phase; DP, delayed phase; ALL, AP + PVP + DP + HBP.		

Table 5  
Coefficient values of the effective texture features in each phase of MRI.

Image	Effective texture features	Coefficient values	
AP	SmallAreaLowGrayLevelEmphasis_glszm_square	0.077156461	
	0.66–0.86	0.63	
		0.712 ± 0.087	
	Skewness_firstorder_wavelet-LHH	0.095294526	
	Skewness_firstorder_wavelet-HLL	0.151447985	
	SmallDependenceEmphasis_gldm_wavelet-HLH	0.02680452	
	SmallAreaEmphasis_glszm_wavelet-HLH	0.117482107	
	SizeZoneNonUniformity_glszm_wavelet-HHH	0.103765611	
	GrayLevelNonUniformity_glszm_wavelet-HHH	0.252583702	
	LowGrayLevelZoneEmphasis_glszm_wavelet-HHH	0.136686495	
	Median_firstorder_wavelet-HHL	0.188192571	
	GrayLevelNonUniformityNormalized_glszm_wavelet-HHL	0.303119702	
	SizeZoneNonUniformityNormalized_glszm_wavelet-HHL	0.323318966	
	ClusterProminence_glcm_wavelet-LLL	0.183118933	
PVP	sex_custom_custom	0.309013968	
	DependenceNonUniformityNormalized_gldm_original	0.335546552	
	Strength_ngtdm_gradient	0.110520859	
	SmallAreaLowGrayLevelEmphasis_glszm_square	0.302579686	
	Kurtosis_firstorder_wavelet-LHH	0.235386934	
	ClusterShade_glcm_wavelet-LHH	0.032810123	
	GrayLevelNonUniformityNormalized_glszm_wavelet-LHH	0.059523649	
	ZoneVariance_glszm_wavelet-HLL	0.168256208	
	Busyness_ngtdm_wavelet-HLL	0.312489979	
	Idn_glcm_wavelet-LLH	0.075028525	
	SmallAreaLowGrayLevelEmphasis_glszm_wavelet-LLH	0.293018721	
	Mean_firstorder_wavelet-HHL	0.275749485	
	DP	ShortRunLowGrayLevelEmphasis_glrIm_original	0.059539585

<b>Image</b>	<b>Effective texture features</b>	<b>Coefficient values</b>
	ClusterShade_glcm_logarithm	0.158903198
	Minimum_firstorder_gradient	0.161657979
	lmc1_glcm_gradient	0.409159357
	RunLengthNonUniformityNormalized_glrIm_gradient	0.177659128
	InverseVariance_glcm_square	0.235843373
	Skewness_firstorder_wavelet-LHH	0.327971754
	LowGrayLevelRunEmphasis_glrIm_wavelet-LHH	0.071209506
	LongRunLowGrayLevelEmphasis_glrIm_wavelet-LHH	0.065713792
	GrayLevelNonUniformity_glszm_wavelet-LLH	0.32810726
	DependenceEntropy_gldm_wavelet-HLH	0.175446267
	SmallDependenceLowGrayLevelEmphasis_gldm_wavelet-HLH	0.341736497
	Contrast_ngtdm_wavelet-HHL	0.457142823
HBP	SmallAreaLowGrayLevelEmphasis_glszm_squareroot	0.184988584
	DependenceVariance_gldm_wavelet-LHL	0.344436616
	LongRunHighGrayLevelEmphasis_glrIm_wavelet-LHL	0.185655045
	DependenceNonUniformityNormalized_gldm_wavelet-LHH	0.181467561
	SmallAreaHighGrayLevelEmphasis_glszm_wavelet-LHH	0.158178023
	ClusterShade_glcm_wavelet-HLL	0.417364813
	ShortRunLowGrayLevelEmphasis_glrIm_wavelet-HLH	0.113996862
	Minimum_firstorder_wavelet-HHH	0.313778167
	SmallAreaLowGrayLevelEmphasis_glszm_wavelet-HHH	0.248887586
ALL	Strength_ngtdm_original	0.017262658
	Busyness_ngtdm_original	0.105281979
	Kurtosis_firstorder_logarithm	0.02032369
	GrayLevelNonUniformity_glszm_logarithm	0.090058042
	Busyness_ngtdm_logarithm	0.034708248
	ShortRunLowGrayLevelEmphasis_glrIm_exponential	0.189230301
	SmallAreaLowGrayLevelEmphasis_glszm_exponential	0.047986854

Image	Effective texture features	Coefficient values
	Minimum_firstorder_gradient	0.271717661
	DependenceVariance_gldm_gradient	0.197013185
	GrayLevelVariance_glszm_gradient	0.258954832
	LargeAreaHighGrayLevelEmphasis_glszm_gradient	0.292767125
	InterquartileRange_firstorder_square	0.26081222
	SmallAreaLowGrayLevelEmphasis_glszm_square	0.125306844
	Busyness_ngtdm_square	0.071149
	InterquartileRange_firstorder_lbp-2D	0.036314475
	Kurtosis_firstorder_lbp-2D	
	Kurtosis_firstorder_lbp-2D	0.024941509
	Skewness_firstorder_wavelet-LHL	0.197202496
	DependenceNonUniformityNormalized_gldm_wavelet-LHL	0.154190974
	RunVariance_glrlm_wavelet-LHL	0.065691314
	Skewness_firstorder_wavelet-LHH	0.073773127
	Mean_firstorder_wavelet-LHH	0.280011474
	MaximumProbability_glcm_wavelet-LHH	0.17535538
	LongRunLowGrayLevelEmphasis_glrlm_wavelet-LHH	0.100042917
	Energy_firstorder_wavelet-LLH	0.108343606
	Idn_glcm_wavelet-LLH	0.115627962
	GrayLevelNonUniformity_gldm_wavelet-LLH	0.023287355
	Strength_ngtdm_wavelet-LLH	0.039249248
	Busyness_ngtdm_wavelet-LLH	0.009143869
	LowGrayLevelZoneEmphasis_glszm_wavelet-HLH	0.196747655
	GrayLevelNonUniformityNormalized_glszm_wavelet-HHH	0.054029792
	SmallAreaLowGrayLevelEmphasis_glszm_wavelet-HHH	0.101657913
	ShortRunEmphasis_glrlm_wavelet-HHL	0.011840098
	LowGrayLevelZoneEmphasis_glszm_wavelet-HHL	0.213536921
	Contrast_ngtdm_wavelet-HHL	0.194934451

Image	Effective texture features	Coefficient values
AP, arterial phase; PVP, portal venous phase; DP, delayed phase; HBP, hepatobiliary phase; ALL, AP + PVP + DP + HBP.		

Table 6

ROC curve analysis parameters of MVI predicted by machine learning modeling of SVM classifier.

<b>Image</b>	<b>SVM/CT training set</b>	<b>SVM/CT validation set</b>	<b>SVM/MRI training set</b>	<b>SVM/MRI validation set</b>
AUC				
AP	0.965	0.842 0.66–0.86	0.962 0.63	0.769
PVP	0.851	0.891 0.81–0.97	0.886 0.88	0.846
DP	0.673	0.643	0.695	0.776
HBP	--	-- 0.79–0.96	0.816 0.70	0.734
ALL	0.864	0.816	0.737	0.640
Sensitivity				
AP	0.979	0.967	0.963	0.846
PVP	0.879	0.984	0.931	0.727
DP	0.700	0.643	0.741	0.692
HBP	--	--	0.759	0.909
ALL	0.786	0.765	0.757	0.754
Specificity				
AP	0.931	0.733	0.897	0.727
PVP	0.759	0.800	0.889	0.846
DP	0.656	0.750	0.759	0.818
HBP	--	--	0.852	0.615
ALL	0.851	0.867	0.719	0.615
Precision				
AP	0.939	0.714	0.923	0.727
PVP	0.784	0.733	0.897	0.667
DP	0.593	0.857	0.727	0.625
				.0.643

Image	SVM/CT	SVM/CT	SVM/MRI	SVM/MRI
	training set	validation set	training set	validation set
HBP	–	–	0.846	0.643
ALL	0.776	0.636	0.773	0.667
95%CI				
AP	0.907–0.986	0.674–0.959	0.906–0.982	0.564–0.945
PVP	0.744–0.957	0.745–0.968	0.784–0.989	0.969–0.988
DP	0.537–0.808	0.417–0.869	0.544–0.845	0.584–0.969
HBP	–	–	0.699–0.933	0.514–0.954
ALL	0.809–0.919	0.719–0.914	0.670–0.803	0.519–0.762
AUC, area under the receiver-operating characteristic curve; 95% CI, 95% confidence interval; AP, arterial phase; PVP, portal venous phase; DP, delayed phase; HBP, hepatobiliary phase; ALL, AP + PVP + DP + HBP; SVM, support vector machine; ROC, receiver-operating characteristic.				

The imaging features extracted from the AP had strong predictive power in both the CT and MRI groups. For the phase images, 15 and 12 valuable features were selected to develop a radiomics signature, respectively. The AUCs of the training set were 0.965 (sensitivity: 0.979; specificity: 0.931; precision: 0.939) and 0.962 (sensitivity: 0.963; specificity: 0.897; precision: 0.923), while the validation set were 0.842 (sensitivity: 0.967; specificity: 0.733; precision: 0.714) and 0.769 (sensitivity: 0.846; specificity: 0.727; precision: 0.727). The PVP also performed well on CT (AUC: 0.851/0.891) and MRI (AUC: 0.886/0.846). The predictive power was not enhanced by combining the features of multi-phase images.

## Discussion

Previous studies have shown that MVI is a major prognostic factor for PLC. For example, Sumie *et al.* found that the degree of MVI is related to the risk of postoperative disease recurrence, and the 2-year tumor-free survival rates of patients without MVI, mild MVI, and severe MVI after hepatectomy were 75.9%, 47.2%, and 32.7%, respectively [11]. Some studies have shown that certain factors affect whether PLC is associated with MVI, including tumor diameter, degree of tumor cell differentiation, AFP level, and the presence of more than one tumor [12]. Proteins induced by the absence of vitamin K or antagonist- $\alpha$  (PIVKA- $\alpha$ ), AFP, alpha-fetoprotein lens culinaris agglutinin 3 (AFP-L3), and  $\gamma$ -glutamyl transpeptidase (GGT), are closely related to MVI [13]. Li *et al.* believed that among HCC patients with histologically-confirmed MVI, the prognosis of patients under 60 years of age was worse than those over 60 years of age [14]. In this study, gender, age, HBsAg, AFP, DCP, and liver cirrhosis status were included as observational indicators. However, there were no statistically significant differences in these indicators between the MVI positive and MVI negative groups. It is inconsistent with the conclusions of previous

studies on the correlation of MVI with AFP and age, which may be related to the small sample size. However, in the MVI positive group, the average age younger than the MVI negative group.

There is a hope that the early prediction of MVI can guide the clinical development of individualized treatment plans. Previously, Kim *et al.* reported that tumor size is correlated with MVI in univariate analyses, but not in multivariate analyses [15]. Some scholars believe that PLC with a diameter of > 5 cm is more likely to spread through MVI [16]. Ahn *et al.* reported that Gd-EOB-DTPA is an important predictor of MVI with tumor enhancement in AP images [17]. Similarly, periarterial enhancement may reflect the effect of MVI on hemodynamics in the peripheral PLC. While normal liver tissue supplies blood to the portal vein, MVI can lead to tumor thrombi formation. In return, small branched embolization of the portal vein may occur around the tumor, followed by a low-perfusion state and arterial hyper-perfusion compensation [18]. In the HBP after Gd-EOB-DTPA enhancement, the contrast agent available to normal hepatocytes showed high signal, while the tumor tissue showed low signal because it did not contain normal hepatocytes and could not absorb the contrast agent. Some scholars have suggested that weak peripheral signal of the hepatobiliary tumor could predict MVI more accurately, as the sensitivity and specificity are higher [15]. In another study, Lee *et al.* speculated that MVI might induce changes in blood perfusion around the tumor, affecting the function of organic anion transport peptides on the liver cell membrane, which is known to introduce Gd-EOB-DTPA into the liver cells. The abnormal function of the translocation polypeptide could reduce the uptake of Gd-EOB-DTPA in the peritumor hepatocytes, leading to a relatively low signal [18].

The tumor size, morphology, and presence of satellite lesions were analyzed on the preoperative enhanced CT images to predict the occurrence of MVI in our study. We found no significant difference in the possibility of MVI, regardless of whether the lesion diameter was greater than 5 cm. Our finding differs from previous studies, which may be related to the small sample size of this study. Meanwhile, we found that the irregular shape of the tumor and the satellite lesions around the tumor were related to the occurrence of MVI. Our study analyzed the differences between the MVI positive group and MVI negative group in fuzzy tumor margins, enhancement around the tumor in the AP, and low signal around the tumor in the HBP on preoperative MRI Gd-EOB-DTPA-enhanced images. In the univariate analysis, the three observation indicators were all related to MVI, which is consistent with previous studies. However, this study's innovation lies in the point-to-point analysis of the seven-point sampling method and MRI analysis. Our conclusions may be more accurate and allow for the avoidance of false-negatives caused by traditional sampling methods.

As a newer field of research, radiomics combines medicine and engineering to convert image information into texture features for quantitative and digital research. In a previous study, Wilson *et al.* extracted texture features from T1, T2, AP, and PVP images of preoperative MRI from patients with HCC. Both tumor entropy and mean were found to be associated with MVI. The texture analysis of preoperative imaging correlated with microscopic features of HCC and can be used to predict patients with high-risk tumors [19]. Another study applied radiomics to analyze the preoperative CT enhanced images of 206 patients with HCC. Different dimensionality-reduction methods and feature classifiers were used for machine

learning, and the efficacies of each model were compared. The models established with the LASSO + GBDT method showed optimal diagnostic performance and the greatest diagnostic value for MVI. Hence, radiomics can be used for the preoperative and noninvasive diagnoses of MVI, yet different dimensionality reduction and modeling methods will affect the final model [20]. In another study, Yang *et al.* established a nomogram model by analyzing the preoperative MRI enhanced images of 208 patients with HCC. They conducted a multi-factor analysis based on the clinical and imaging characteristics of patients. The nomogram that incorporated the clinicopathologic risk factors and radiomic features derived from the HBP images achieved satisfactory preoperative prediction of the individualized risk of MVI in patients with HCC [21].

In our study, we conducted a point-to-point comparison analysis of the imaging and pathology of patients with PLC, delineated the ROI of the corresponding regions for pathological sampling, and extracted the corresponding texture features to establish a radiomics model to predict the occurrence of MVI. SVM feature classifiers were used for machine learning, and good predictive effects were obtained in the AP of preoperative CT and MRI images. The model established in this study avoided the error caused by inconsistencies between pathological sampling and image control.

## Limitations

The sample size of this study was small. Still, we believe that the results obtained were highly accurate with the cooperation of intraoperative positioning by clinicians and postoperative sampling by pathologists. In return, we believe that our study has prevented the occurrence of false positives. In future work, we plan to improve our multidisciplinary cooperation further, while also expanding our sample sizes.

## Conclusions

This was a retrospective study on preoperative imaging (CT and MRI) and radiomics, based on a seven-point pathological sampling method, which can avoid false-negative results commonly associated with conventional pathological sampling methods. In return, the imaging analysis results and the established radiomics prediction model may be more accurate. In the preoperative CT imaging features, irregular morphology, and satellite lesions around the tumor were found to be associated with the occurrence of MVI. In terms of preoperative MRI, MVI was correlated with fuzzy tumor boundaries, peripheral enhancement in the AP, and peripheral low signal in the HBP. We established the radiomics model by comparing the CT and MRI images with the pathological findings and used SVM feature classifiers for machine learning. In return, our model showed good predictive efficacy in the AP of preoperative CT and MRI images, which could aid in the development of individualized treatment plans for patients with PLC in the future.

## Abbreviations

MVI: microvascular infiltration

PLC: primary liver cancer

SVM: support vector machine

AP: arterial phase

PVP: portal venous phase

DP: delayed phase

HBP: hepatobiliary phase

HBsAg: hepatitis b surface antigen

AFP: alpha-fetoprotein

DCP: des- $\gamma$ -carboxy Prothrombin

## Declarations

**Ethics approval and consent to participate** We confirm that all methods were carried out in accordance with relevant guidelines and regulations, and all experimental protocols were approved by the Director of Ethical Review Committee of The First Affiliated Hospital of Guangxi Medical University, and informed consent was obtained from all subjects.

**Consent for publication** The data and images in this study have deleted the information of patients, protecting the privacy of patients, and can be used for publication.

**Availability of data and materials** The data that support the findings of this study are available from Huiying Medical Technology, but restrictions apply to the availability of these data, which were used under license for the current study, and so are not publicly available. Data are however available from the authors upon reasonable request and with permission of Fang Wang and Yuwei Xia.

**Competing interests** There is no financial or non-financial competing interests in this study.

**Funding** National Scientific and Natural Foundation of China 82060310

**Authors' contributions** Xialing Huang and Liling Long contributed to the methods of this study. Xinping Ye and Zili Lv contributed to the operation of the study. Ling Zhang, Muliang Jiang and Yidi Chen contributed to the data collection of this study. Fang Wang and Yuwei Xia contributed to the data analysis of the study. Xialing Huang, Jieqin Wei and Liling Long contributed to writing this manuscript.

**Acknowledgements**—Many thanks to all those who contributed to this study, including method design, data collection, surgical localization, pathologic tracking, and paper writing. Thanks also to the team for the language polishing of the manuscript.

## References

- [1] Banerjee S, Wang DS, Kim HJ, et al. A computed tomography radiogenomic biomarker predicts microvascular invasion and clinical outcomes in hepatocellular carcinoma. *HEPATOLOGY* 2015;62(3):792-800.
- [2] Unal E, Idilman IS, Akata D, et al. Microvascular invasion in hepatocellular carcinoma. *DIAGN INTERV RADIOL* 2016;22(2):125-32.
- [3] Du M, Chen L, Zhao J, et al. Microvascular invasion (MVI) is a poorer prognostic predictor for small hepatocellular carcinoma. *BMC CANCER* 2014;14:38.
- [4] Hirokawa F, Hayashi M, Asakuma M, et al. Risk factors and patterns of early recurrence after curative hepatectomy for hepatocellular carcinoma. *SURG ONCOL* 2016;25(1):24-9.
- [5] Rodriguez-Peralvarez M, Luong TV, Andreana L, et al. A systematic review of microvascular invasion in hepatocellular carcinoma: diagnostic and prognostic variability. *ANN SURG ONCOL* 2013;20(1):325-39.
- [6] Zhao W, Liu W, Liu H, et al. Preoperative prediction of microvascular invasion of hepatocellular carcinoma with IVIM diffusion-weighted MR imaging and Gd-EOB-DTPA-enhanced MR imaging. *PLOS ONE* 2018;13(5):e197488.
- [7] Chetty R. Surgical pathology dissection. An illustrated guide, 2nd ed. *Journal of Clinical Pathology* 2004;57(6):672-672.
- [8] Wu MC, Tang ZY, Liu YY, et al. Guidelines for diagnosis and treatment of primary liver cancer in China (2019 edition). *Chinese Journal of Hepatology* 2020;28(2):112-128.
- [9] Lahan-Martins D, Perales SR, Gallani SK, et al. Microvascular invasion in hepatocellular carcinoma: is it predictable with quantitative computed tomography parameters? *Radiol Bras* 2019;52(5):287-92.
- [10] Feng ST, Jia Y, Liao B, et al. Preoperative prediction of microvascular invasion in hepatocellular cancer: a radiomics model using Gd-EOB-DTPA-enhanced MRI. *EUR RADIOL* 2019;29(9):4648-59.
- [11] Sumie S, Nakashima O, Okuda K, et al. The significance of classifying microvascular invasion in patients with hepatocellular carcinoma. *ANN SURG ONCOL* 2014;21(3):1002-9.
- [12] Hameed B, Mehta N, Sapisochin G, et al. Alpha-fetoprotein level > 1000 ng/mL as an exclusion criterion for liver transplantation in patients with hepatocellular carcinoma meeting the Milan criteria. *Liver Transpl* 2014;20(8):945-51.

- [13] Pote N, Cauchy F, Albuquerque M, et al. Performance of PIVKA-II for early hepatocellular carcinoma diagnosis and prediction of microvascular invasion. *J HEPATOL* 2015;62(4):848-54.
- [14] Li L, Xu L, Wen T, et al. Poor Prognoses of Young Hepatocellular Carcinoma Patients with Microvascular Invasion: A Propensity Score Matching Cohort Study. *Gastroenterol Res Pract* 2020;2020:4691425.
- [15] Kim KA, Kim MJ, Jeon HM, et al. Prediction of microvascular invasion of hepatocellular carcinoma: usefulness of peritumoral hypointensity seen on gadoxetate disodium-enhanced hepatobiliary phase images. *J MAGN RESON IMAGING* 2012;35(3):629-34.
- [16] Renzulli M, Brocchi S, Cucchetti A, et al. Can Current Preoperative Imaging Be Used to Detect Microvascular Invasion of Hepatocellular Carcinoma? *RADIOLOGY* 2016;279(2):432-42.
- [17] Ahn SY, Lee JM, Joo I, et al. Prediction of microvascular invasion of hepatocellular carcinoma using gadoxetic acid-enhanced MR and (18)F-FDG PET/CT. *ABDOM IMAGING* 2015;40(4):843-51.
- [18] Lee S, Kim SH, Lee JE, et al. Preoperative gadoxetic acid-enhanced MRI for predicting microvascular invasion in patients with single hepatocellular carcinoma. *J HEPATOL* 2017;67(3):526-34.
- [19] Wilson GC, Cannella R, Fiorentini G, et al. Texture analysis on preoperative contrast-enhanced magnetic resonance imaging identifies microvascular invasion in hepatocellular carcinoma. *HPB (Oxford)* 2020.
- [20] Ni M, Zhou X, Lv Q, et al. Radiomics models for diagnosing microvascular invasion in hepatocellular carcinoma: which model is the best model? *CANCER IMAGING* 2019;19(1):60.
- [21] Yang L, Gu D, Wei J, et al. A Radiomics Nomogram for Preoperative Prediction of Microvascular Invasion in Hepatocellular Carcinoma. *Liver Cancer* 2019;8(5):373-86.

## Figures

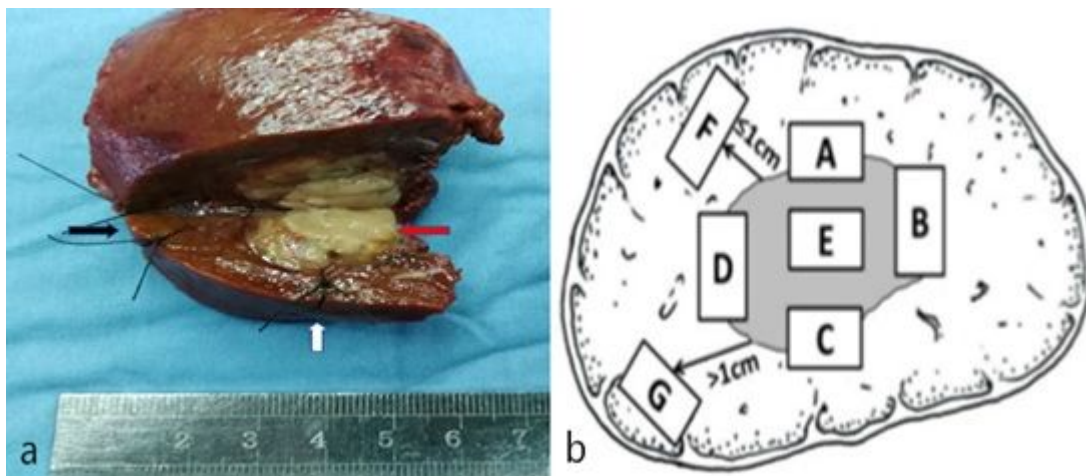


## Figure 1

Localization of seven points in gross liver specimens. a: Intraoperative localization of gross liver cancer specimens, where a suture line represents the front of the body (white arrow); two sutures represent the right side of the body (black arrow); and the largest area of the lesion was incised along the transverse direction of the human body (red arrow). b: Schematic diagram of the seven sampling sites of the pathological specimen. A, B, C, and D are at the 12, 3, 6, and 9 o'clock locations of the maximum tumor section, and the sampling at the junction of carcinoma and para-carcinoma liver tissue is 1:1. F represents a piece of liver tissue from the tumor margin  $\leq 1$  cm (near the tumor), while G represents a piece of liver tissue  $> 1$  cm from the edge of the tumor (far from the tumor).

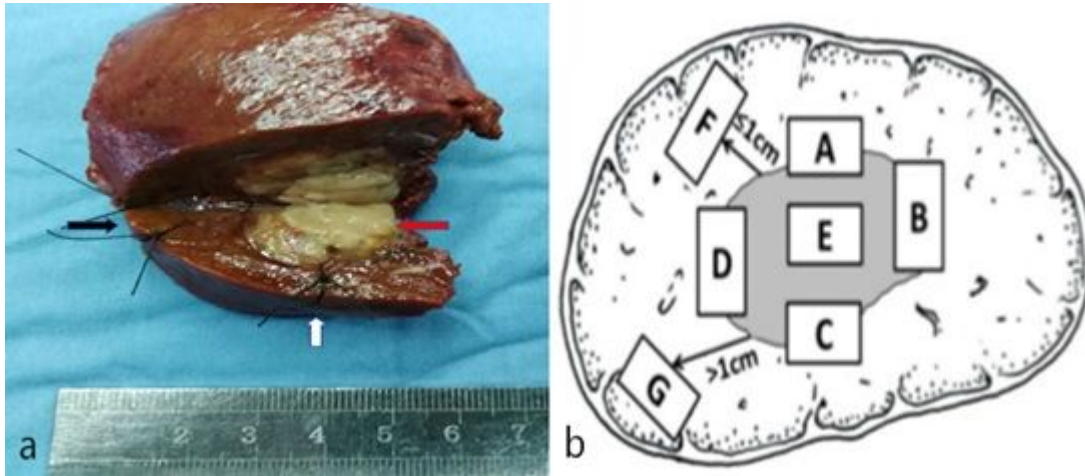


## Figure 1

Localization of seven points in gross liver specimens. a: Intraoperative localization of gross liver cancer specimens, where a suture line represents the front of the body (white arrow); two sutures represent the right side of the body (black arrow); and the largest area of the lesion was incised along the transverse direction of the human body (red arrow). b: Schematic diagram of the seven sampling sites of the pathological specimen. A, B, C, and D are at the 12, 3, 6, and 9 o'clock locations of the maximum tumor section, and the sampling at the junction of carcinoma and para-carcinoma liver tissue is 1:1. F represents a piece of liver tissue from the tumor margin  $\leq 1$  cm (near the tumor), while G represents a piece of liver tissue  $> 1$  cm from the edge of the tumor (far from the tumor).

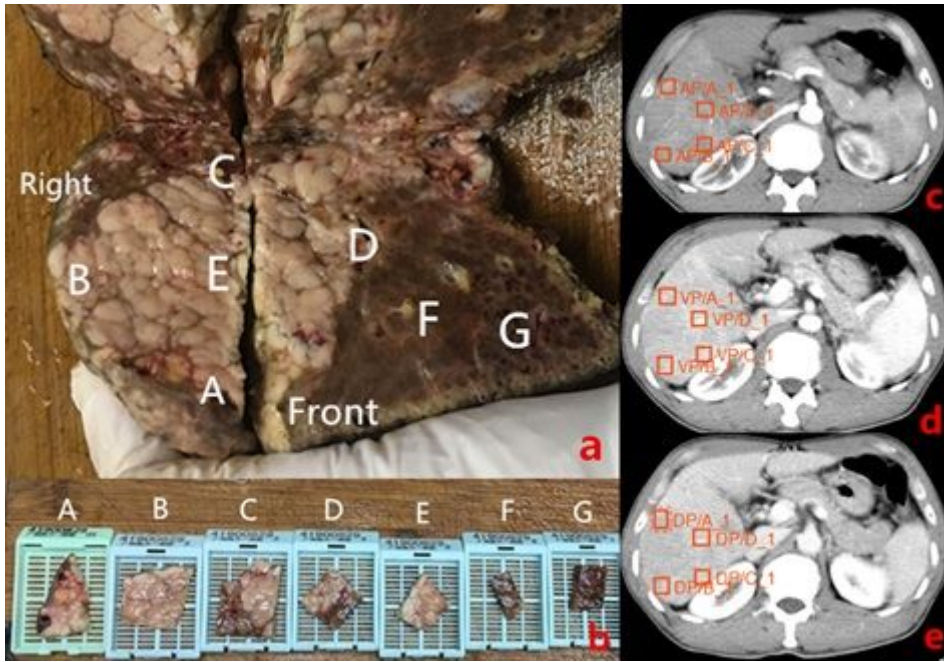


**Figure 2**

ROI delineated by pathological sampling and CT comparison. a: The gross liver cancer specimens were sampled at seven points in the maximum cross-section. b: The corresponding tissue specimen after pathological sampling. c, d, and e: ROIs were delineated at points A, B, C, and D, which corresponded to the pathological specimens in the AP, PVP, and DP of CT images. AP, arterial phase; PVP, portal venous phase; DP, delayed phase; ROI, region of interest.

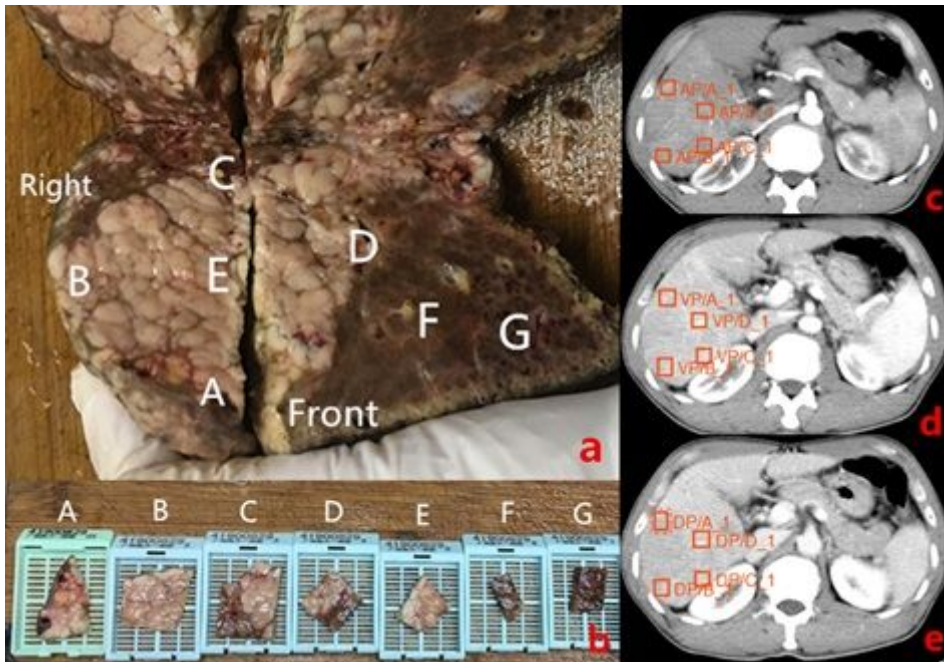


**Figure 2**

ROI delineated by pathological sampling and CT comparison. a: The gross liver cancer specimens were sampled at seven points in the maximum cross-section. b: The corresponding tissue specimen after

pathological sampling. c, d, and e: ROIs were delineated at points A, B, C, and D, which corresponded to the pathological specimens in the AP, PVP, and DP of CT images. AP, arterial phase; PVP, portal venous phase; DP, delayed phase; ROI, region of interest.

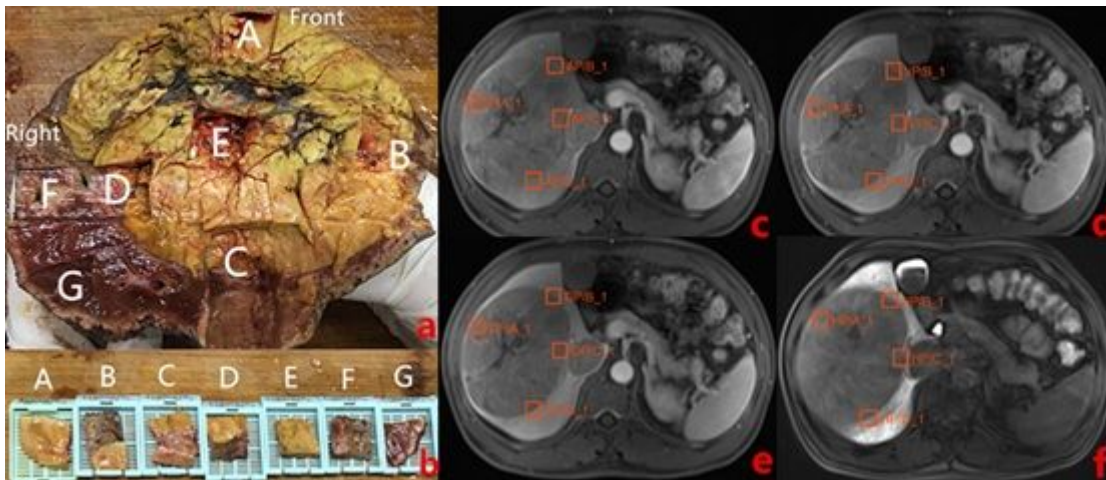


**Figure 3**

ROI delineated by pathological sampling and MRI comparisons. a: The gross liver cancer specimens were sampled at seven points in the maximum cross-section. b: The corresponding tissue specimen after pathological sampling. c, d, e, and f: ROIs were delineated at points A, B, C, and D, which corresponded to the pathological specimens in the AP, PVP, DP, and HBP of MRI images. AP, arterial phase; PVP, portal venous phase; DP, delayed phase; HBP, hepatobiliary phase; ROI, region of interest.

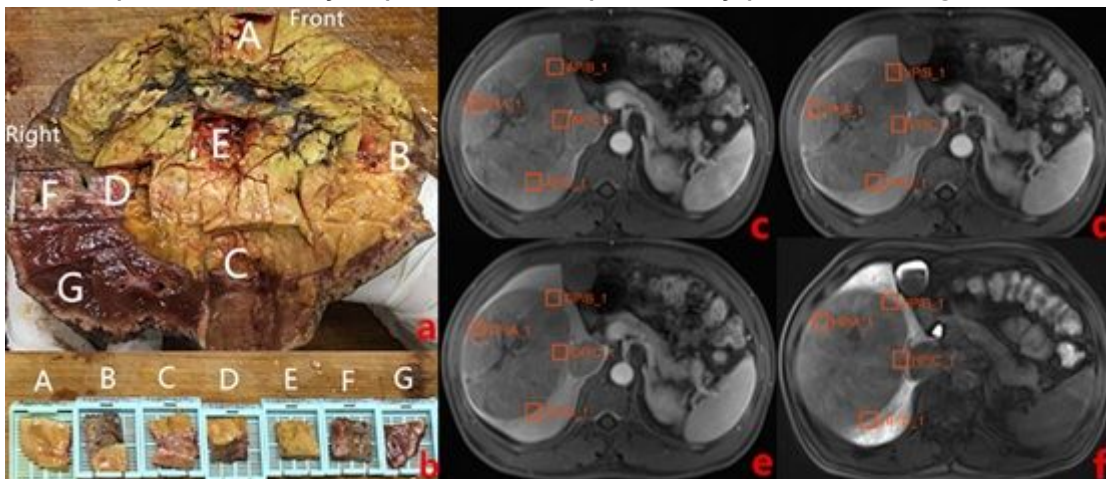


**Figure 3**

ROI delineated by pathological sampling and MRI comparisons. a: The gross liver cancer specimens were sampled at seven points in the maximum cross-section. b: The corresponding tissue specimen after pathological sampling. c, d, e, and f: ROIs were delineated at points A, B, C, and D, which corresponded to the pathological specimens in the AP, PVP, DP, and HBP of MRI images. AP, arterial phase; PVP, portal venous phase; DP, delayed phase; HBP, hepatobiliary phase; ROI, region of interest.

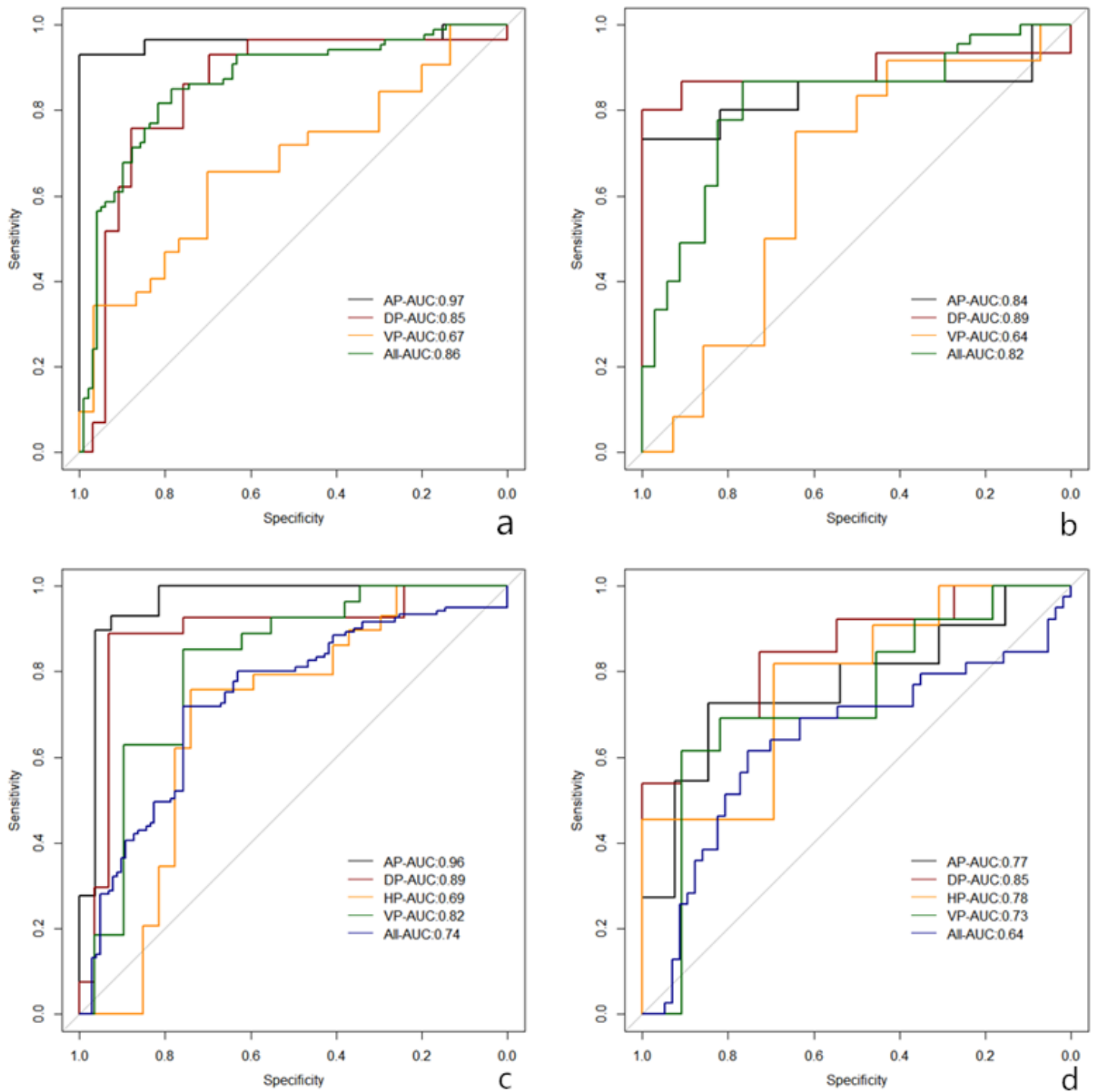


**Figure 4**

The ROC analysis of SVM on different phases in the MRI and CT datasets. a: The ROC curve of the training set in the CT (AP: arterial phase, VP: portal venous phase, DP: delayed phase, All: AP+VP+DP); b: The ROC curve of the validation set in the CT. c: The ROC curve of the training set in the MRI (HP: hepatobiliary phase, ALL: AP+VP+DP+HP); d: The ROC curve of the validation set in the MRI

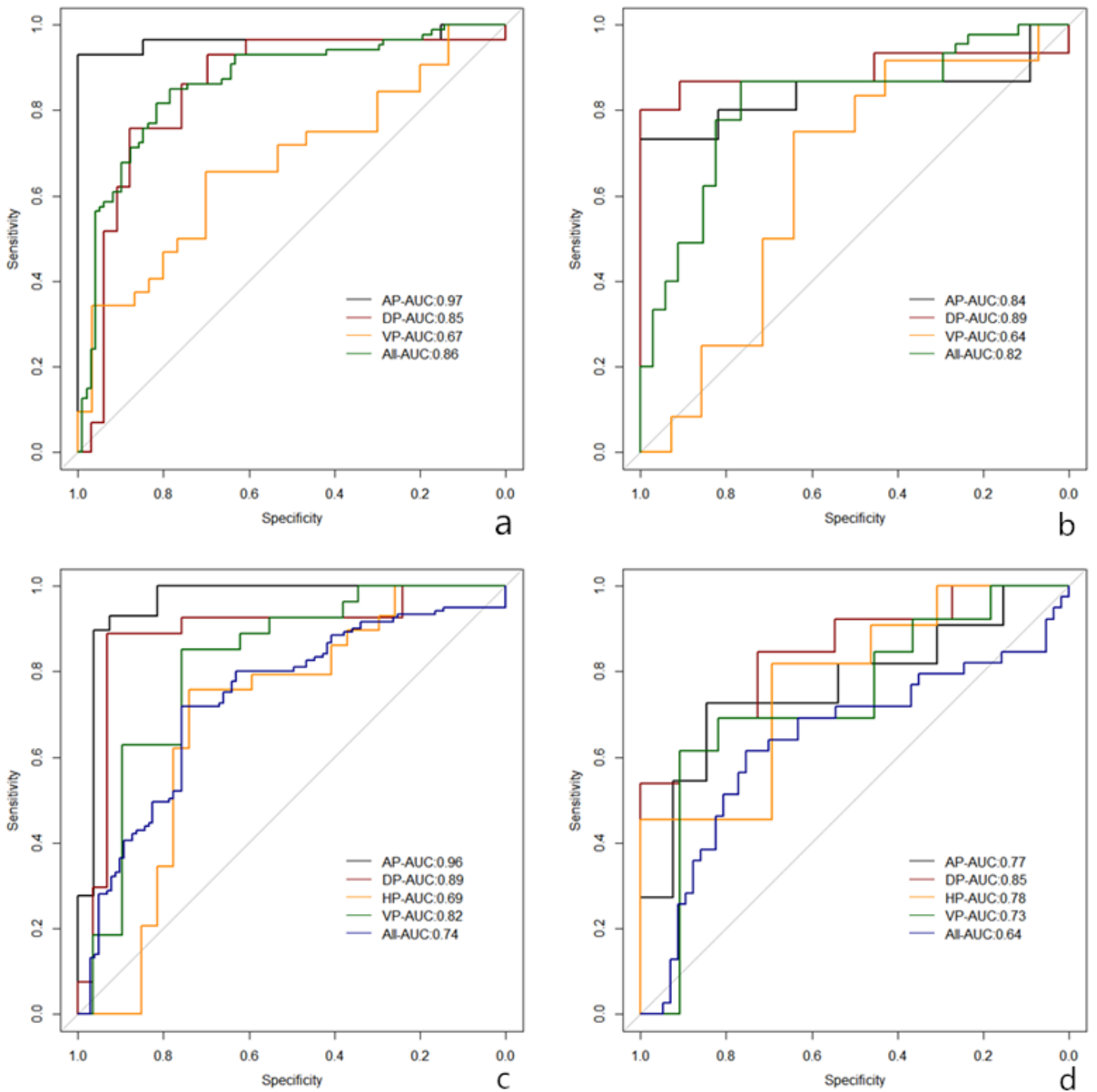


**Figure 4**

The ROC analysis of SVM on different phases in the MRI and CT datasets. a: The ROC curve of the training set in the CT (AP: arterial phase, VP: portal venous phase, DP: delayed phase, All: AP+VP+DP); b: The ROC curve of the validation set in the CT. c: The ROC curve of the training set in the MRI (HP: hepatobiliary phase, ALL: AP+VP+DP+HP); d: The ROC curve of the validation set in the MRI